

www.acsami.org Research Article

Stabilizing Hydrogen Adsorption through Theory-Guided Chalcogen Substitution in Chevrel-Phase Mo₆X₈ (X=S, Se, Te) Electrocatalysts

Jessica C. Ortiz-Rodríguez, Nicholas R. Singstock, Joseph T. Perryman, Forrest P. Hyler, Sarah J. Jones, Aaron M. Holder, Charles B. Musgrave, and Jesús M. Velázquez*



Cite This: ACS Appl. Mater. Interfaces 2020, 12, 35995–36003



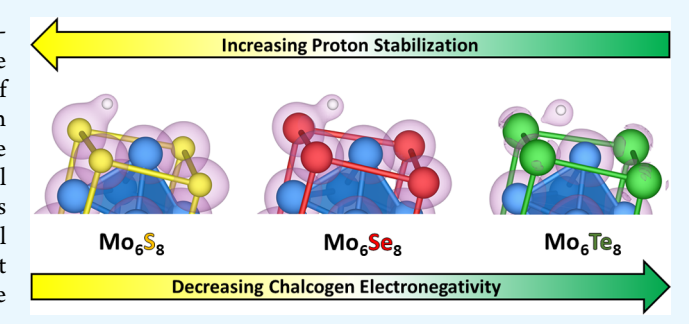
ACCESS

Metrics & More

Article Recommendations

s Supporting Information

ABSTRACT: In this work, we implement a facile microwave-assisted synthesis method to yield three binary Chevrel-Phase chalcogenides (Mo_6X_8 ; X = S, Se, Te) and investigate the effect of increasing chalcogen electronegativity on hydrogen evolution catalytic activity. Density functional theory predictions indicate that increasing chalcogen electronegativity in these materials will yield a favorable electronic structure for proton reduction. This is confirmed experimentally via X-ray absorption spectroscopy as well as traditional electrochemical analysis. We have identified that increasing the electronegativity of X in Mo_6X_8 increases the hydrogen adsorption strength owing to a favorable shift in the p-



band position as well as an increase in the Lewis basicity of the chalcogen, thereby improving hydrogen evolution reaction energetics. We find that Mo_6S_8 exhibits the highest hydrogen evolution activity of the Mo_6X_8 series of catalysts, requiring an overpotential of 321 mV to achieve a current density of 10 mA cm⁻²_{ECSA}, a Tafel slope of 74 mV per decade, and an exchange current density of 6.01 \times 10⁻⁴ mA cm⁻²_{ECSA}. Agreement between theory and experiment in this work indicates that the compositionally tunable Chevrel-Phase chalcogenide family is a promising framework for which electronic structure can be predictably modified to improve catalytic small-molecule reduction reactivity.

KEYWORDS: Chevrel-Phase chalcogenides, microwave-assisted solid-state synthesis, electronic structure, adsorption free energy, hydrogen evolution, electrocatalysis

1. INTRODUCTION

Renewable hydrogen production has become an attractive alternative to transition away from fossil fuels and reduce carbon dioxide emissions. In addition to its high gravimetric energy density as well as the environment friendliness of its combustion product, hydrogen is attractive due to its role in industrial processes such as ammonia synthesis, hydrogenation reactions, crude oil refining, and biogas processing. Currently, hydrogen gas is predominantly generated via steam methane reforming, which leads to substantial anthropogenic CO₂ emission. Alternatively, hydrogen can be generated via electrochemical water splitting—a process that leaves virtually no carbon footprint when coupled to renewable sources of electricity such as wind and solar energy. This electrochemical process occurs according to the half-reaction

$$2H^{+} + 2e^{-} \rightleftharpoons H_{2} \tag{1}$$

Following Sabatier's principle for heterogeneous catalysis, the Gibbs free energy for hydrogen adsorption of a maximally efficient hydrogen evolution reaction (HER) catalyst will be thermoneutral ($\Delta G_{\rm H} \approx 0$). While Pt is currently championed as the most efficient HER catalyst owing to its nearly thermoneutral H adsorption, scalability of systems based

Received: April 19, 2020 Accepted: July 15, 2020 Published: July 15, 2020





compounds relies on the negatively polarized chalcogenide anions, which results in lower free-energy barriers for proton adsorption. 27

To investigate the effect of electronic structure and active-site coordination on chemically analogous earth-abundant catalysts, we examined Chevrel-Phase (CP) chalcogenides with the generic formula $M_y Mo_6 X_8$ (M= alkali, alkaline, transition or post-transition metals, y=0-4; X=S, Se, Te), specifically focusing on the binary $Mo_6 X_8$. This chalcogenide family is especially attractive due to its interconnected cluster framework (Figure 1) and its tunable composition that affords fine control over the electronic structure, which has led to previously observed catalytic activity for hydrodesulfurization, oxygen reduction, $^{31-35}$ and CO_2 reduction reactions. 36

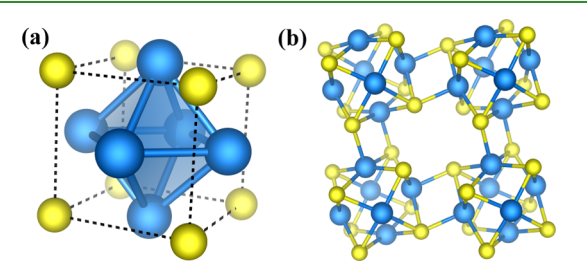


Figure 1. Structure of the binary CP chalcogenides depicting (a) Mo_6X_8 unit cell with the metallic Mo–Mo bonds of the octahedra shown within the chalcogenide cage, as indicated by the dashed lines, and (b) four Mo_6X_8 units illustrating the ionic Mo–X bonds within and between the clusters, and the large cavities formed between clusters.

Metal-intercalated CP frameworks have been shown to be stable and relatively active HER catalysts over a range of operating conditions;^{31,37–39} however, the effect of chalcogen composition on HER reactivity in CPs is not well understood. We hypothesized that the electronegative chalcogenide surface sites would bond with adsorbed hydrogen and that varying the chalcogen identity would directly affect the strength of this bond, as well as shifting the position of the Mo d-states relative to the Fermi level. Density functional theory (DFT) calculations support this hypothesis and provide additional insight into the contributions of both the local coordination environment and the bulk electronic structure to H adsorption and suggest that the p-band center provides a useful descriptor for bond strength. To confirm the results of DFT calculations, we implemented a time- and energy-efficient synthetic method to yield all three binary CP chalcogenide compositions. Predicted changes to CP electronic structure were confirmed experimentally via X-ray absorption spectroscopy (XAS) and were correlated to changes in catalytic HER reactivity under acidic operating conditions. The results presented herein offer insights into the tunability of electrocatalytic reactivity exhibited by CP chalcogenides, and our integrated theoretical and experimental effort represents a promising route toward rational and iterative material design driven by reliable computational prediction.

2. EXPERIMENTAL SECTION

2.1. Chemicals and Materials. MoS_2 powder (99%, ~325 mesh), Cu powder (99.995%, ~100 mesh), $MoSe_2$ powder (99.999%, ~200 mesh), and Pt mesh (99.99%) were used as purchased from Alfa Aesar. Mo powder (99.99%, ~100 mesh), Te powder (99.8%,

 $\sim\!200$ mesh), and concentrated $\rm H_2SO_4$ acid (ACS grade) were used as purchased from Sigma-Aldrich. Fused quartz tubes (2 mm thick) were purchased from AdValue Technology and made into round-bottom tubes with an in-house oxy-hydrogen torch. Ultrahigh purity grade $\rm H_2$ (99.999%) was used as purchased from Praxair Direct. Toray Carbon Paper (060 with Micro Porous Layer) and 20% Pt/C on Vulcan Carbon Cloth were purchased from Fuel Cell Store. Ag/AgCl reference electrodes were purchased through ALS Japan. Selemion anion exchange membrane was purchased from AGC Engineering and stored in ultrapure deionized water prior to use in electrochemical experiments.

2.2. Catalyst Synthesis. The CP chalcogenides studied here were synthesized using a high-temperature heating method described in detail in our previous work. ^{36,40} Briefly, appropriate precursor powders were mixed via ball-milling and pressed into pellets, transferred into quartz tubes under N₂ under tightly packed Al₂O₃ microfiber, then submerged in a bath of ~325 mesh graphite powder in a conventional microwave oven under Ar where the samples were irradiated for multiple minutes at a power of up to 1000 W. As the electronegativity of the chalcogen decreases, the number of electrons per Mo₆ cluster increases up to a limit of 24 electrons for a completely filled valence shell.⁴¹ The increase in valence electron count when less electronegative chalcogens are incorporated leads to an increase in cluster stability and decreases the heating time required to obtain phase-pure CPs. This is particularly important for Mo₆S₈, where owing to the electron-withdrawing strength of S-the Mo₆ octahedron is slightly electron-deficient at 20e-, making the cluster metastable and prone to decomposition under the high-temperature conditions of this synthetic method. To mitigate the destabilizing effects of this electron deficiency, a metallic Cu precursor was included to stabilize the Mo₆ octahedron in a Cu₂Mo₆S₈ framework. The heating time required to produce Mo₆Te₈, Mo₆Se₈, and Cu₂Mo₆S₈ varied from 5, 8, and 10 min, respectively. To obtain deintercalated Mo₆S₈, Cu was chemically etched in O₂-bubbled 6.0 M HCl according to the literature methods.4

2.3. Structural and Electronic Characterization. The phase purity of CPs was analyzed via powder X-ray diffraction (PXRD) using a Bruker D8 Advance diffractometer with Cu K α radiation (1.541 Å). Catalyst morphology and bulk composition were analyzed before and after electrolysis using a FEI (Hillsboro, OR) 430 nanoSEM scanning electron microscope and a FEI Scios DualBeam scanning electron microscope with an Oxford energy dispersive X-ray (EDX) detector, respectively. Surface composition analysis before and after electrolysis was completed using a PHI Versaprobe 3 X-ray photoelectron spectrometer.

2.4. XAS and Data Analysis. CP chalcogenides were all scanned at their respective Mo L_3 -edge. All XAS scans were taken at the Stanford Synchrotron Radiation Lightsource (SSRL) at the SLAC National Accelerator Laboratory. Mo₆Se₈ scans were taken at beamline 14–3, while Mo₆S₈ and Mo₆Te₈ scans were performed at beamline 4–3. All edge scans were performed under He with a chamber O₂ content <0.04% in order to minimize interactions between tender X-rays and the gas inside the sample chamber. Energy calibration of the beam was performed using elemental Mo foil. For each sample, fluorescence data were collected using a Lytle detector over the course of three scans which were averaged together to improve the signal-to-noise ratio.

2.5. Electrochemical Characterization. Electrochemical measurements were performed in a custom three-electrode H-shaped cell (Figure S1) where the working-electrode and counter-electrode compartments were separated by an anion-exchange membrane. Working electrodes were fabricated using powder-based inks for each catalyst prepared using 3.0 mL of isopropanol, 50 μ L of polytetrafluoroethylene (PTFE) suspension, 5 mg of carbon black, and 6.01×10^{-5} mol of each respective catalyst. The PTFE serves as a binding agent while the carbon black increases conductivity. The PTFE/carbon black mixture facilitates the transport of the evolving hydrogen from the reaction site through hydrophobic pores and provides robust mechanical properties to the electrode. 43,44 Inks were sonicated for 20 min and then drop cast onto conductive carbon

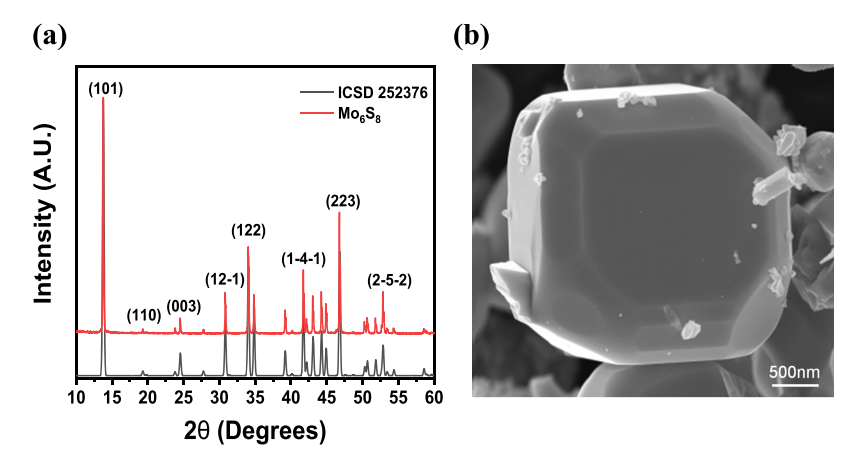


Figure 2. (a) PXRD patterns for Mo_6S_8 comparing experimental (red) and calculated pattern based on published data (black) and (b) SEM micrograph detailing the faceted morphology of polycrystalline Mo_6S_8 .

paper (Figure S2). The working (CP), reference (Ag/AgCl), and counter (Pt mesh) electrodes were submerged in 0.5 M $\rm H_2SO_4$ electrolyte that was purged with $\rm H_2$ gas for 30 min to remove any dissolved $\rm O_2$. All electrochemical experiments were performed using a Bio-Logic VSP-300 multichannel potentiostat with potentials converted to RHE scale using the following equation

$$E_{\text{RHE}} = E(Ag/AgCl) + 0.210 + 0.059 \times \text{pH}$$
 (2)

Hydrogen evolution activity was evaluated via linear sweep voltammetry (LSV) at a scan rate of 5 mV $\rm s^{-1}$. During these experiments, a H2 flow was maintained over the electrolyte and the electrolyte was stirred at 1200 rpm to remove hydrogen gas bubbles from the working electrode surface and maintain consistent local pH. Catalyst stability was observed in two different experiments for each catalyst: (1) chronopotentiometry experiments where a specific current density was maintained over time while observing changes in overpotential and (2) LSV experiments performed both before and after 500 and 1000 cyclic voltammograms. Electrochemically active surface area (ECSA) for each electrode was determined by measuring their double-layer capacitance (C_{dl}) , whereas cyclic voltammograms (CVs) were acquired at various scan rates in a non-Faradaic region where observable current could be attributed strictly to capacitive charging. 45 The current at a chosen potential near open circuit in these CVs was plotted as a function of scan rate, and the slope of this graph gives C_{dl}. Figures S3 and S4 show the representative CVs and linear plots used to calculate $C_{\rm dl}$. The intrinsic $C_{\rm dl}$ of each catalyst was taken as the difference of the $C_{\rm dl}$ of the electrode (PTFE/carbon black/catalyst) and the $C_{\rm dl}$ of the blank (PTFE/carbon black). The ECSA was then calculated by dividing C_{dl} by the specific capacitance (C_s) of the sample

$$ECSA = \frac{C_{DL}}{C_{s}}$$
(3)

where a specific capacitance of 60 $\mu\mathrm{F}$ cm⁻² was chosen based on the reported capacitance for a flat MoS_2 sample in 0.5 M $\mathrm{H}_2\mathrm{SO}_4$. Charge-transfer resistance was measured via electrochemical impedance spectroscopy (EIS) at -0.27 V versus RHE with a superimposed AC bias oscillating at frequencies from 1 MHz to 1 Hz with a 10 mV sinus amplitude.

2.6. Computational Methods and Models. DFT calculations were performed using the Vienna ab initio Simulation Package (VASP).⁴⁷ The Revised Perdew–Burke–Ernzerhof (RPBE)⁴⁸ generalized gradient approximation exchange–correlation functional was used to compute structures and zero-point energies, while the Strongly Constrained and Appropriately Normed (SCAN) semilocal density functional⁴⁹ was used to compute enthalpies, charge densities, and densities of states (DOS). All calculations were performed with a plane-wave cutoff of 520 eV and a Γ-centered Monkhorst–Pack *k*-point grid with a density of 1000/*N* where *N* is the number of atoms

in the unit cell. All calculations were performed using the implicit water solvation model as implemented in VASPsol. Sol. Zero-point energies were calculated using the dynamical matrix approach within Henkelman's VTST Tools package. Charge densities were calculated using DDEC6 atomic population analysis. Sol.

Adsorption energies at 298.15 K are calculated using

$$\Delta G_{\rm ads} = \Delta H_{\rm ads} + \Delta E_{\rm ZPE} - T \Delta S_{\rm ads} \tag{4}$$

Adsorption enthalpies are calculated with

$$\Delta H_{\rm ads} = H_{\rm ads} - H_{\rm surf} - 1/2H_{\rm H_2} \tag{5}$$

where $H_{\rm ads}$, $H_{\rm surf}$ and $H_{\rm H_2}$ are the computed total enthalpies of the surface with an adsorbate, the bare surface, and $\rm H_2$, respectively. The change in zero-point energy is calculated using

$$\Delta E_{\rm ZPE} = E_{\rm ZPE,H^*} - \frac{1}{2} E_{\rm ZPE,H_2}$$
 (6)

where $E_{\rm ZPE,H^*}$ is the zero-point energy of adsorbed hydrogen (H*), and $E_{\rm ZPE,H_2}$ is the experimental zero-point energy of H₂ (0.27 eV). We make the approximation that

$$T\Delta S_{\rm ads} \approx -\frac{1}{2}S_{\rm H_2std}$$
 at 298.15 K (7)

because the vibrational entropy of H* is negligibly small relative to hydrogen in solution. 53 $S_{\rm H_2 std}$ = 0.4038 eV is obtained from the National Institute of Standards and Technology Joint Army–Navy–Air Force (NIST JANAF) thermochemical database. 54 Periodic slab models of the surfaces included a 1 \times 1 \times 2 supercell model of the Mo₆X₈ surface and a 2 \times 2 \times 3 supercell model of the (111) Pt surface due to its smaller unit cell size to reduce adsorbate—adsorbate interactions. All models for adsorption on Mo₆X₈ include one H* per supercell due to the unfavorable adsorption of H* on these materials. Additionally, these calculations included one H₂O adsorbed at the Mo surface site due to the favorable adsorption of H₂O on these surfaces. The Pt surface was modeled at 1/4, 1/2, 3/4, and full surface coverages of H*. Slab calculations included 20 Å of solvent above the slab in the z-direction to avoid interactions between periodic images.

3. RESULTS AND DISCUSSION

3.1. Microwave-Assisted Solid-State Synthesis. Polycrystalline Mo₆S₈, Mo₆Se₈, and Mo₆Te₈ were all synthesized with high phase-purity through aforementioned methods. This work presents for the first time microwave-assisted high-temperature methods extended to Mo₆Se₈ and Mo₆Te₈. In contrast to conventional heating, which relies on slow heat transfer through evacuated quartz ampules, the microwave heating method employed here allows for rapid conversion of

microwave radiation into thermal energy, 55 and the N_2 atmosphere within the reaction vessel itself allows for virtually instantaneous heat transfer to the sample. Because of the rapid nature of this microwave heating, reaction times to obtain CPs are reduced from days to minutes, resulting in significant time and energy savings despite the required high temperatures (>900 °C). Furthermore, the yield of this solid-state synthesis method is 100%, making it advantageous compared to many solution-based methods where unreacted precursors and product loss during separation often reduces overall yield.

The PXRD pattern for Mo₆S₈ shown in Figure 2a indicates a rhombohedral crystal phase with an intense (101) signal that is characteristic of CPs, while the scanning electron microscopy (SEM) image in Figure 2b details the faceted polycrystalline morphology that is representative of the CPs studied in this work. The PXRD patterns, X-ray photoelectron spectroscopy (XPS) spectra, and EDX spectra (Figure S5) obtained before and after chemical etching confirm the complete removal of Cu from the Mo₆S₈ framework. PXRD and SEM of CP selenides and tellurides (Figure S6) show similar characteristic diffraction peaks and polycrystalline morphology. Lattice parameters obtained by PXRD refinement for CP chalcogenides are shown in Table S1 and are consistent with literature values for the R-3H unit cell. Bulk CP composition was confirmed via EDX, as shown in Figures S7-S9. For Mo₆S₈₁ the Mo L- and S K-edges overlap, convoluting quantitative determination of Mo and S, hence the reported atomic % deviates significantly from expected values; although it is apparent from the EDX spectra presented in Figure S7 that there is no compositional impurities.

3.2. Electronic Structure and Theoretical H* Interaction. The Mo L₃-edge X-ray absorption near edge structure (XANES) for all three CPs are shown in Figure 3 and reveal

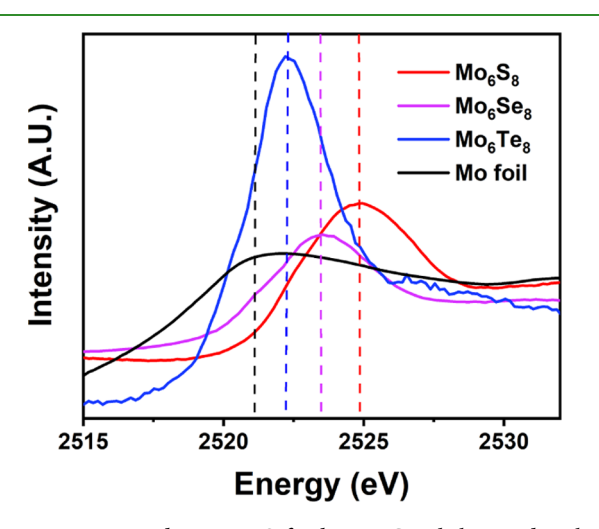


Figure 3. Mo L_3 -Edge XANES for binary CP chalcogenides along with a Mo foil for reference, illustrating a pronounced red-shift as chalcogen electronegativity decreases from Mo_6S_8 (red) to Mo_6Te_8 (blue).

that as the electronegativity of the chalcogen species decreases, the photon energy required to induce a $2p \rightarrow 4d$ transition similarly decreases, suggesting a less oxidized Mo center which is the result of weaker electron withdrawal from Mo_6 by the X_8 cage. This is indicative that a more electronegative chalcogen strongly decreases the valence electron count of the Mo_6 octahedron, which makes the chalcogen a stronger Lewis

base that will stabilize the absorbed proton more effectively during HER because H⁺ is a hard Lewis acid. DFT calculations support this explanation.

Calculated Gibbs free energies for proton adsorption ($\Delta G_{\rm H}$) on CP chalcogenides are shown in Figure 4a along with Pt for reference. As expected, Pt exhibits the most favorable H* binding interaction, while for CP chalcogenides, Mo₆S₈ is predicted to possess the most favorable $\Delta G_{\rm H}$, followed by Mo₆Se₈ and Mo₆Te₈ with $\Delta G_{\rm H}$ of 0.48, 0.56, and 0.58 eV, respectively. The lower $\Delta G_{\rm H}$ obtained for Mo₆S₈ corroborates our hypothesis that a stronger Lewis base adjacent to Mo stabilizes H* more effectively, thereby facilitating HER reaction kinetics. Furthermore, our calculations indicate that the most favorable adsorption site for all three CP surfaces is the bridge site between Mo and X, which can be seen in the slab images of Figure S10 where H* is stabilized closest to X in Mo₆S₈ (X-H distance = 1.40 Å) and farthest from X in Mo₆Te₈ (X-H distance = 1.81 Å).

To further examine how the electronic structures of the CPs influence their reactivity, projected DOS were calculated for each material and are plotted in Figure 4b. As the electronegativity of the chalcogen increases, the d-band center energy decreases, suggesting a weaker interaction between H* and the Mo d-states. This result is consistent with the longer Mo-H bond calculated for Mo₆S₈. Conversely, the X-H bond strengthens as chalcogen electronegativity increases, and to a greater extent than the Mo-H bond weakens. This results in stronger overall adsorption of H* predicted for Mo₆S₈. We attribute the stronger X-H bond for the more electronegative chalcogens to both local and bulk electronic effects. The local contribution to the X-H bond strength results from orbital overlap which decreases with orbital size mismatch between the chalcogen and the H* 1s orbital (e.g., large mismatch between Te 5s and H 1s). The bulk contribution results from the charge density localization on the chalcogen atoms which increases with the electronegativity of X and is manifested in the electronic structure as a lower p-band center. The increased charge density on X leads to stronger bonding with H* and concomitantly decreases the charge density on Mo, weakening the Mo-H bond. To assess the influence of the local and bulk contributions on the strength of the X-H bond, we studied the effect of substituting only the chalcogen involved in the X-H bond with a different chalcogen. Three substitutions were considered: Se into Mo₆S₈, S into Mo₆Se₈, and S into Mo₆Te₈. The calculated ΔH_{ads} for these substitutions are shown in Figure S11. We report calculated bond lengths, band centers, charge densities, and ΔH_{ads} in Table S2. These substitutions change the local bonding environment, yet have a minimal effect on the bulk electronic structure, exhibited by the negligible change in the d-band and p-band centers (<0.05 eV), as well as by the negligible change in Mo charge densities. The Se substitution into Mo₆S₈ increases $\Delta H_{\rm ads}$ by 0.08 eV resulting in an adsorption enthalpy that is only 0.03 eV lower than that of bulk Mo₆Se₈. Additionally, the Se-H bonds of both structures differ by only 0.01 Å, indicating that the local bonding environment influences the X-H bond strength more than the bulk electronic structure.

The S substitutions into Mo_6Se_8 and Mo_6Te_8 decrease ΔH_{ads} by 0.03 and 0.02 eV, respectively. The difference between ΔH_{ads} for the S substitution into Mo_6Se_8 and the Se substitution into Mo_6S_8 is less than 0.01 eV. However, the S–H bond is 0.14 Å shorter than the Se–H bond, further

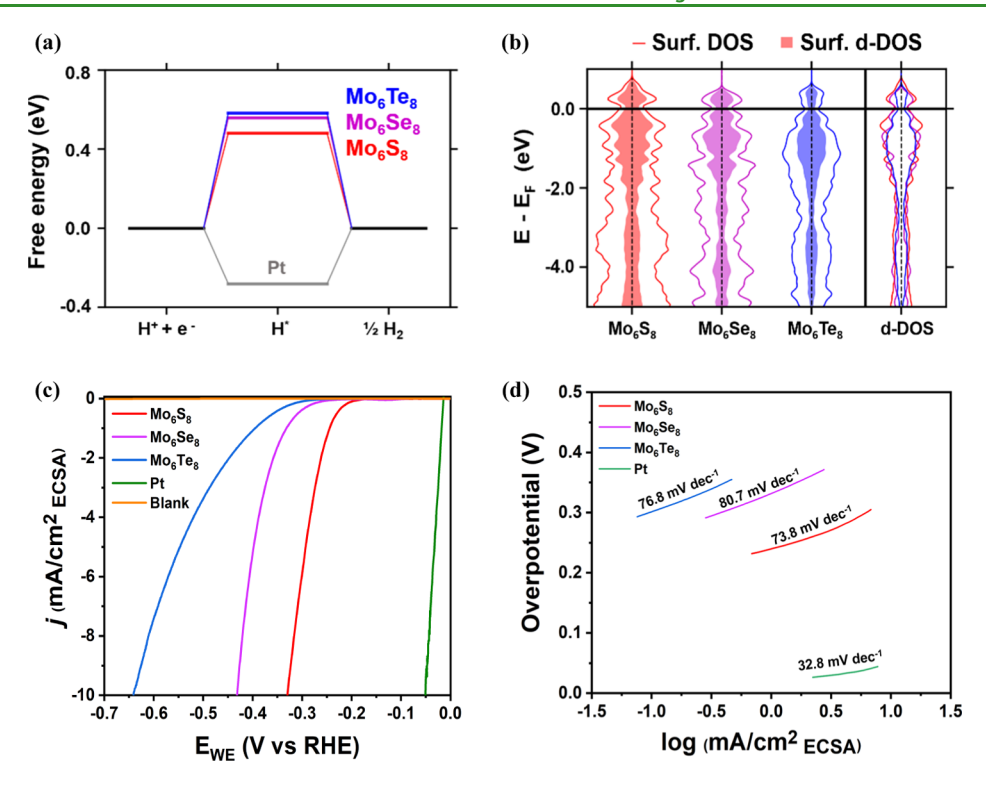


Figure 4. (a) Calculated adsorption energies of H^* (ΔG_H) on all surfaces discussed herein; (b) computed DOS which indicate a significantly larger d-DOS at the Fermi level for Mo_6Se_8 than for Mo_6Se_8 and Mo_6Te_8 ; (c) HER polarization curves for CP chalcogenide electrodes in 0.5 M H_2SO_4 , along with 20% Pt/C on Vulcan carbon cloth and a blank (carbon paper with PTFE/carbon black/IPA ink) for comparison; and (d) corresponding Tafel plots for each CP catalyst, with Pt for comparison.

confirming that the local bonding environment contributes more substantially to the X–H bond strength, although the overall proton adsorption strength is comparable. Nonetheless, when comparing Mo_6S_8 against the two S substitutions into Mo_6Se_8 and Mo_6Te_8 , $\Delta H_{\rm ads}$ increases by 0.07 and 0.12 eV, respectively, indicating that the bulk electronic structure moderately affects the adsorption strength of the proton, which can be stabilized by decreasing the p-band center. The individual tunability of the local bonding environment and bulk electronic structure suggests that the ternary CP space may include promising HER catalysts with optimal properties for H adsorption. Furthermore, of the three chalcogenides S provides the best local bonding environment and bulk electronic structure for stabilizing H*, in agreement with our calculations that Mo_6S_8 exhibits the lowest $\Delta G_{\rm H}$ of the binary CPs.

3.3. Electrochemical HER Activity. Polarization curves in 0.5 M H₂SO₄ and Tafel slopes for all three CP chalcogenides are shown in Figure 4c,d along with curves for 20% Pt/C on Vulcan Carbon Cloth and a blank for reference, while numerical figures of merit are shown in Table 1. Current densities were normalized with respect to ECSA to account for

Table 1. Compiled figures of Merit for all Three Binary CPs Studied Herein

Material	$ \begin{array}{c} j \text{ at} \\ -10 \text{ mA cm}^{-2}_{\text{ECSA}} \\ (\text{mV}) \end{array} $	Tafel slope (mV dec ⁻¹)	Exchange current density (mA cm ⁻² _{ECSA})	$R_{\mathrm{ct}} \ (\Omega)$
Mo_6S_8	321	74	6.01×10^{-4}	3.2
Mo_6Se_8	432	81	9.57×10^{-5}	154.4
Mo_6Te_8	634	77	3.01×10^{-5}	446.0

any slight differences in particle sizes of the catalysts that were evaluated. Because of the ease with which tellurium compounds oxidize in air, Mo₆Te₈ electrodes were treated prior to electrolysis to ensure that the catalytic activity recorded came from Mo₆Te₈ and not the oxide. The Mo₆Te₈ electrodes were submerged in 0.5 M H₂SO₄ for 30 min. Under these acidic conditions, ${\rm TeO_2}$ spontaneously dissolves in the form of the telluryl ion, ${\rm HTeO_2}^+$ This ion further reduces to elemental tellurium under negative applied potential; therefore, following this 30 min dissolution period the electrolyte was replaced while continuously purging the cell with hydrogen to prevent re-oxidation of the electrode surface. The overpotential required to achieve a current density of 10 mA cm⁻² $_{ECSA}$ follows the trend: Mo₆S₈ < Mo₆Se₈ < Mo₆Te₈, with values of 321, 432, and 634, respectively, indicating that on an energy-input basis, Mo₆S₈ is the most efficient of the three catalysts studied. In addition, an overpotential of 265 mV is required to achieve 10 mA cm⁻² on a geometric basis for Mo₆S₈, which is consistent with many commonly reported bulk and nanostructured earth-abundant HER catalysts for which current density is normalized with respect to geometric surface area, as shown in Table S3. $^{22,46,58-61}$ Considering that the HER activity of Mo₆S₈ was measured using bulk polycrystalline catalyst material, considerable opportunity exists to improve the overpotential required to achieve a current density of 10 mA cm⁻² through dimensional reduction, as has been successful in many other HER catalyst materials such as MoS₂. 46

The observed HER behavior agrees with the measured trend in Mo L-edge position across the three binary CPs, as coordination of Mo to an increasingly electronegative X species will yield a harder X_8 cage that favors H^* stabilization.

Catalytic activity also agrees with calculated $\Delta G_{\rm H}$, confirming the effect $\Delta G_{\rm H}$ plays on reaction kinetics. The Tafel slopes obtained for CP chalcogenides are all significantly higher than the Tafel slope for platinum, which suggests that the reaction proceeds via a Volmer–Heyrovsky mechanism that involves electrochemical desorption during a concerted proton-coupled electron transfer as the final step toward $\rm H_2$ production. The endergonic $\Delta G_{\rm H}$ for all three CPs suggests low H* surface coverage, further supporting a Volmer–Heyrovsky mechanism. The lower $\Delta G_{\rm H}$ obtained for $\rm Mo_6S_8$ agrees with its lower Tafel slope, which indicates fast proton adsorption followed by a sluggish desorption step, higher desorption due to their higher adsorption free energy.

To further investigate HER kinetics over CP electrocatalyst surfaces, EIS was performed to measure charge-transfer resistance (R_{ct}) at -0.27 V versus RHE as shown in Figure S12. The considerable increase R_{ct} from Mo₆S₈ (40.2 Ω) to Mo₆Te₈ (436.0 Ω) suggests significantly more sluggish kinetics as the electronegativity of the chalcogen decreases, which is to be expected based on previously discussed trends in the electronic structure.

Cycling stability as shown in Figures 5a and S13 indicates an increase in overpotential to achieve 10 mA cm $^{-2}$ after 1000 cycles of 5 mV for Mo₆S₈, 15 mV for Mo₆Se₈, and 16 mV for

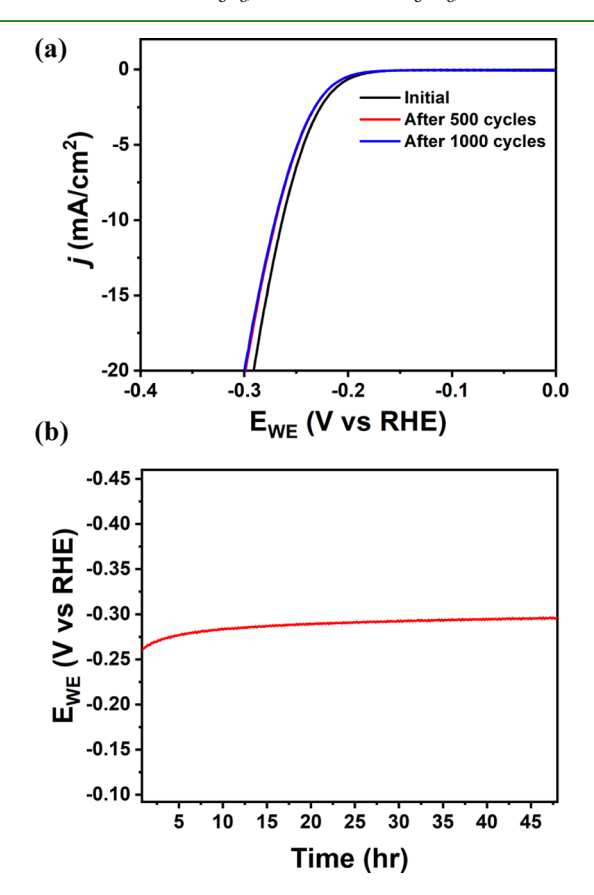


Figure 5. (a) HER polarization curves for Mo_6S_8 recorded before (black) and after 500 (red) and 1000 (blue) potential sweeps from 0.0 to -0.4 V vs RHE in 0.5 M H_2SO_4 with current normalized with respect to geometric surface area and (b) chronopotentiometry experiment with an Mo_6S_8 electrode illustrating a steady time-dependent overpotential at a current density of 10 mA cm⁻² over 48 h.

Mo₆Te₈; hence, Mo₆S₈ appears to be the most robust of the three CP compositions studied. EDX spectra for the binary CPs reveal consistent bulk composition of the catalysts after cycling, while SEM images indicate no significant changes to the morphology or distribution of catalyst on the surface over the course of electrolysis for the sulfides and selenides (Figures S7 and S8). In the case of the tellurides, SEM images show a significant decrease in the surface coverage over the course of electrolysis (Figure S9). We hypothesize that this is a result of weaker interactions between Mo₆Te₈ and the PTFE binding agent, making it less mechanically robust under the electrolysis conditions. XPS spectra shown in Figures S14-S16 indicate the presence of a native oxide layer that is significantly smaller after electrolysis on Mo₆S₈ and Mo₆Se₈ but slightly larger for Mo₆Te₈ as a result of the ease with which tellurium is oxidized under ambient conditions. However, it appears that the surface Mo and X composition is relatively consistent over the course of electrolysis, and because of the pre-treatment used for the CP tellurides, it is unlikely that any native oxide persists under electrolysis conditions.

In order to confirm the apparent stability of the Mo_6S_8 composition, chronopotentiometry experiments were performed where current density was maintained at 10 mA cm⁻² for 48 h in order to observe overpotential as a function of electrolysis time. Figure 5b shows that the overpotential for Mo_6S_8 was steady even over the course of extended periods of electrolysis. The PXRD pattern for the Mo_6S_8 electrode before electrolysis (Figure S17) reveals the characteristic (101) signal of CPs, which remains after 48 h of electrolysis without any significant changes in the diffraction pattern. Figures S18 and S19 show XPS spectra and SEM images of the electrode, respectively, which further confirm consistent catalyst composition and morphology over the course of prolonged electrolysis.

It is clear from the electrochemical and spectroscopic analyses presented here that $\mathrm{Mo_6S_8}$ is the most promising binary CP catalyst composition, owing to its increased X site basicity that promotes favorable HER kinetics. This was also found to be the most stable composition of all three CPs and is, therefore, a promising candidate for systematic electronic structure and electrocatalytic evaluation following ternary element intercalation between $\mathrm{Mo_6X_8}$ units. Furthermore, CP sulfides have also been shown to be stable under reductive applied bias in basic conditions, ^{37,39} which extends the range of conditions in which ternary phases can be evaluated.

4. CONCLUSIONS

This work represents the first systematic study of the effect of chalcogen substitution on HER activity in acidic conditions for CP chalcogenide catalysts. It is also the first extension of microwave-assisted solid-state heating to molybdenum selenide and telluride materials. The result of Mo L-edge XAS for the three binary catalysts studied here reflects an expected increase in chalcogen basicity as the electron-withdrawing nature of the chalcogen increases, which leads to increased HER reactivity, in good agreement with fundamental hard-soft acid-base theory. The CP catalysts with more electronegative chalcogen species stabilized H* at HER-active Mo-X bridging sites more effectively, resulting in greatly improved HER activity for Mo₆S₈ compared to Mo₆Se₈ and Mo₆Te₈. DFT calculations indicate that this stabilization is due to a stronger X-H bond, which results from improved orbital overlap and a lower bulk p-band center. Furthermore, our calculations indicate that the

position of the p-band center can be independently tuned to stabilize H* adsorption. Therefore, we conclude that for the binary CPs, the position of the p-band center is a useful descriptor of the catalytic activity for HER which may provide critical insights for identifying ternary CP compositions with improved HER activity, and for investigating more complicated catalytic reactions where H adsorption is an important elementary step (e.g., electrochemical ${\rm CO_2}$ and ${\rm CO}$ reduction). The p-band center may also prove to be a useful descriptor for catalytic activity of other transition-metal chalcogenides.

Experimental characterization confirmed predictions from theory, indicating that HER activity decreases as the electronegativity of the chalcogen decreases. Mo₆S₈ exhibited an overpotential of 321 mV at 10 mA cm⁻²_{ECSA} compared to 432 and 634 mV for Mo₆Se₈ and Mo₆Te₈, respectively. Tafel slopes in the range of 74–82 mV dec⁻¹ for all CPs indicate that the rate-limiting step for all three compositions is electrochemical desorption as part of the Volmer-Heyrovsky mechanism. It is apparent from the strong agreement between our theoretical predictions and experimental characterization that HER activity in CP chalcogenides can be predictably affected by catalyst composition. This observation paves the way for future studies on the effect of ternary elementintercalation into CPs on catalytic activity and may ultimately lead to an effective method for predicting and analyzing new compositions of optimally reactive CP catalyst materials.

ASSOCIATED CONTENT

Supporting Information

The Supporting Information is available free of charge at https://pubs.acs.org/doi/10.1021/acsami.0c07207.

Schematic of the electrochemical setup and electrode preparation setup; representative CVs of CP chalcogenides in a non-faradaic region; representative doublelayer capacitance calculations; XPS and EDX survey scan of Cu₂Mo₆S₈ and Mo₆S₈ obtained after chemical etching; PXRD and SEM for Mo₆Se₈ and Mo₆Te₈ powders; EDX spectra for Mo₆Te₈ electrode before and after electrolysis; computationally predicted binding geometry for Hads on CP chalcogenides; calculated $\Delta H_{\rm ads}$ in CP chalcogenides along with substitution of the chalcogen involved in the X-H bond for a different chalcogen; Nyquist plots for CP chalcogenides; polarization curves for Mo₆Te₈ and Mo₆Te₈ inks after 500 and 1000 cyclic voltammograms; XPS spectra before and after electrolysis for Mo₆Te₈; PXRD for Mo₆S₈ electrode before and after chronopotentiometry over 48 h; SEM images for Mo₆S₈ electrode before and after chronopotentiometry over 48 h; lattice parameters for all CP chalcogenides; DFT calculated properties for CP chalcogenides; and comparison of the overpotentials of earth-abundant HER catalysts in acidic media (PDF)

AUTHOR INFORMATION

Corresponding Authors

Aaron M. Holder — Department of Chemical and Biological Engineering, University of Colorado at Boulder, Boulder, Colorado 80309, United States; orcid.org/0000-0002-1878-1541; Email: aaron.holder@colorado.edu

Charles B. Musgrave — Department of Chemical and Biological Engineering and Department of Chemistry, University of

Colorado at Boulder, Boulder, Colorado 80309, United States; orcid.org/0000-0002-5732-3180;

Email: charles.musgrave@colorado.edu

Jesús M. Velázquez — Department of Chemistry, University of California Davis, Davis, California 95616, United States; orcid.org/0000-0003-2790-0976; Email: jevelazquez@ucdavis.edu

Authors

Jessica C. Ortiz-Rodríguez – Department of Chemistry, University of California Davis, Davis, California 95616, United States

Nicholas R. Singstock — Department of Chemical and Biological Engineering, University of Colorado at Boulder, Boulder, Colorado 80309, United States

Joseph T. Perryman – Department of Chemistry, University of California Davis, Davis, California 95616, United States

Forrest P. Hyler – Department of Chemistry, University of California Davis, Davis, California 95616, United States

Sarah J. Jones – Department of Chemistry, Pomona College, Claremont, California 91711-6338, United States

Complete contact information is available at: https://pubs.acs.org/10.1021/acsami.0c07207

Author Contributions

⁸J.C.O-R. and N.R.S contributed equally to this manuscript. All authors have given approval to the final version of the manuscript.

Notes

The authors declare no competing financial interest.

ACKNOWLEDGMENTS

We would like to acknowledge the University of California, Davis for start-up funding, as well as support from the Cottrell Scholar program supported by the Research Corporation for Science Advancement (RCSA grant ID#26780). We also acknowledge funding support from the NSF through UC Davis ChemEnergy REU program, grant #1560479 2) the NSF Graduate Research Fellowship, grant # 1650042. J.T.P. thanks Chevron Corporation for funding through the UC Davis Institute of Transportation Chevron fellowship program. C.B.M. and N.R.S. were supported by the NSF (Awards CBET-1806079 and CHE-1800592). N.R.S. was also supported by a U.S. Department of Education Graduate Assistance in Areas of National Need Fellowship under the Materials for Energy Conversion and Sustainability program. Part of this work was performed at the Stanford Nano Shared Facilities (SNSF), supported by the National Science Foundation under award ECCS-1542152. This research used resources of the National Energy Research Scientific Computing Center, a DOE Office of Science User Facility supported by the Office of Science of the U.S. Department of Energy under contract no. DE-AC02-05CH11231 (project ID: 60905). The use of Stanford Synchrotron Radiation Lightsource, SLAC National Accelerator Laboratory, is supported by the U.S. Department of Energy, Office of Science, Office of Basic Energy Sciences under Contract No. DE-AC02-76SF00515. The SSRL Structural Molecular Biology Program is supported by the DOE Office of Biological and Environmental Research, and by the National Institutes of Health, National Institute of General Medical Sciences (including P41GM103393). The contents of this publication are solely the responsibility of the authors and

do not necessarily represent the official views of NIGMS of NIH.

REFERENCES

- (1) Sharma, S.; Ghoshal, S. K. Hydrogen the Future Transportation Fuel: From Production to Applications. *Renewable Sustainable Energy Rev.* **2015**, *43*, 1151–1158.
- (2) Davis, S. J.; Lewis, N. S.; Shaner, M.; Aggarwal, S.; Arent, D.; Azevedo, I. L.; Benson, S. M.; Bradley, T.; Brouwer, J.; Chiang, Y.-M.; Clack, C. T. M.; Cohen, A.; Doig, S.; Edmonds, J.; Fennell, P.; Field, C. B.; Hannegan, B.; Hodge, B.-M.; Hoffert, M. I.; Ingersoll, E.; Jaramillo, P.; Lackner, K. S.; Mach, K. J.; Mastrandrea, M.; Ogden, J.; Peterson, P. F.; Sanchez, D. L.; Sperling, D.; Stagner, J.; Trancik, J. E.; Yang, C.-J.; Caldeira, K. Net-Zero Emissions Energy Systems. *Science* 2018, 360, No. eaas9793.
- (3) Ayers, K. Gigawatt-Scale Renewable Hydrogen via Water Splitting as a Case Study for Collaboration: The Need to Connect Fundamental and Applied Research to Accelerate Solutions. *MRS Energy Sustain.* **2017**, *4*, No. E11.
- (4) Baroutaji, A.; Wilberforce, T.; Ramadan, M.; Olabi, A. G. Comprehensive Investigation on Hydrogen and Fuel Cell Technology in the Aviation and Aerospace Sectors. *Renewable Sustainable Energy Rev.* **2019**, *106*, 31–40.
- (5) Spath, P. L.; Mann, M. K. Life Cycle Assessment of Hydrogen Production via Natural Gas Steam Reforming; National Renewable Energy Laboratory, 2001, Report No. TP-570-27637.
- (6) Shamsi, H.; Haghi, E.; Raahemifar, K.; Fowler, M. Five-Year Technology Selection Optimization to Achieve Specific CO₂ Emission Reduction Targets. *Int. J. Hydrogen Energy* **2019**, *44*, 3966–3984.
- (7) Ludwig, J. R.; Schindler, C. S. Catalyst: Sustainable Catalysis. Chem 2017, 2, 313–316.
- (8) Abbas, M. A.; Bang, J. H. Rising Again: Opportunities and Challenges for Platinum-Free Electrocatalysts. *Chem. Mater.* **2015**, 27, 7218–7235.
- (9) Evans, D. J.; Pickett, C. J. Chemistry and the Hydrogenases. Chem. Soc. Rev. 2003, 32, 268-275.
- (10) Rees, D. C.; Howard, J. B. The Interface Between the Biological and Inorganic Worlds: Iron-Sulfur Metalloclusters. *Science* **2003**, *300*, 929–931.
- (11) Hinnemann, B.; Moses, P. G.; Bonde, J.; Jørgensen, K. P.; Nielsen, J. H.; Horch, S.; Chorkendorff, I.; Nørskov, J. K. Biomimetic Hydrogen Evolution: MoS₂ Nanoparticles as Catalyst for Hydrogen Evolution. *J. Am. Chem. Soc.* **2005**, *127*, 5308–5309.
- (12) Jaramillo, T. F.; Jørgensen, K. P.; Bonde, J.; Nielsen, J. H.; Horch, S.; Chorkendorff, I. Identification of Active Edge Sites for Electrochemical H₂ Evolution from MoS₂ Nanocatalysts. *Science* **2007**, 317, 100–102.
- (13) Norskov, J. K.; Abild-Pedersen, F.; Studt, F.; Bligaard, T. Density Functional Theory in Surface Chemistry and Catalysis. *Proc. Natl. Acad. Sci. U.S.A.* **2011**, *108*, 937–943.
- (14) Voiry, D.; Yamaguchi, H.; Li, J.; Silva, R.; Alves, D. C. B.; Fujita, T.; Chen, M.; Asefa, T.; Shenoy, V. B.; Eda, G.; Chhowalla, M. Enhanced Catalytic Activity in Strained Chemically Exfoliated WS₂ Nanosheets for Hydrogen Evolution. *Nat. Mater.* **2013**, *12*, 850–855.
- (15) Cheng, L.; Huang, W.; Gong, Q.; Liu, C.; Liu, Z.; Li, Y.; Dai, H. Ultrathin WS₂ Nanoflakes as a High-Performance Electrocatalyst for the Hydrogen Evolution Reaction. *Angew. Chem., Int. Ed.* **2014**, *53*, 7860–7863.
- (16) Miao, R.; Dutta, B.; Sahoo, S.; He, J.; Zhong, W.; Cetegen, S. A.; Jiang, T.; Alpay, S. P.; Suib, S. L. Mesoporous Iron Sulfide for Highly Efficient Electrocatalytic Hydrogen Evolution. *J. Am. Chem. Soc.* **2017**, *139*, 13604–13607.
- (17) Fan, M.; Zhang, L.; Li, K.; Liu, J.; Zheng, Y.; Zhang, L.; Song, S.; Qiao, Z.-A. FeS₂@C Core-Shell Nanochains as Efficient Electrocatalysts for Hydrogen Evolution Reaction. *ACS Appl. Nano Mater.* **2019**, *2*, 3889–3896.
- (18) Faber, M. S.; Dziedzic, R.; Lukowski, M. A.; Kaiser, N. S.; Ding, Q.; Jin, S. High-Performance Electrocatalysis Using Metallic Cobalt

- Pyrite (CoS₂) Micro- and Nanostructures. *J. Am. Chem. Soc.* **2014**, 136, 10053–10061.
- (19) Wang, A.; Zhang, M.; Li, H.; Wu, F.; Yan, K.; Xiao, J. Combination of Theory and Experiment Achieving a Rational Design of Electrocatalysts for Hydrogen Evolution on the Hierarchically Mesoporous CoS₂ Microsphere. *J. Phys. Chem. C* **2019**, *123*, 13428–13433.
- (20) Wang, H.; Kong, D.; Johanes, P.; Cha, J. J.; Zheng, G.; Yan, K.; Liu, N.; Cui, Y. MoSe₂ and WSe₂ Nanofilms with Vertically Aligned Molecular Layers on Curved and Rough Surfaces. *Nano Lett.* **2013**, 13, 3426–3433.
- (21) Yin, Y.; Zhang, Y.; Gao, T.; Yao, T.; Zhang, X.; Han, J.; Wang, X.; Zhang, Z.; Xu, P.; Zhang, P.; Cao, X.; Song, B.; Jin, S. Synergistic Phase and Disorder Engineering in 1T-MoSe₂ Nanosheets for Enhanced Hydrogen-Evolution Reaction. *Adv. Mater.* **2017**, *29*, 170031.
- (22) Kong, D.; Wang, H.; Cha, J. J.; Pasta, M.; Koski, K. J.; Yao, J.; Cui, Y. Synthesis of MoS₂ and MoSe₂ Films with Vertically Aligned Layers. *Nano Lett.* **2013**, *13*, 1341–1347.
- (23) Zhang, X.-L.; Hu, S.-J.; Zheng, Y.-R.; Wu, R.; Gao, F.-Y.; Yang, P.-P.; Niu, Z.-Z.; Gu, C.; Yu, X.; Zheng, X.-S.; Ma, C.; Zheng, X.; Zhu, J.-F.; Gao, M.-R.; Yu, S.-H. Polymorphic Cobalt Diselenide as Extremely Stable Electrocatalyst in Acidic Media via a Phase-Mixing Strategy. *Nat. Commun.* **2019**, *10*, 5338.
- (24) Zheng, Y.-R.; Wu, P.; Gao, M.-R.; Zhang, X.-L.; Gao, F.-Y.; Ju, H.-X.; Wu, R.; Gao, Q.; You, R.; Huang, W.-X.; Liu, S.-J.; Hu, S.-W.; Zhu, J.; Li, Z.; Yu, S.-H. Doping-Induced Structural Phase Transition in Cobalt Diselenide Enables Enhanced Hydrogen Evolution Catalysis. *Nat. Commun.* **2018**, *9*, 2533.
- (25) Wang, K.; Ye, Z.; Liu, C.; Xi, D.; Zhou, C.; Shi, Z.; Xia, H.; Liu, G.; Qiao, G. Morphology-Controllable Synthesis of Cobalt Telluride Branched Nanostructures on Carbon Fiber Paper as Electrocatalysts for Hydrogen Evolution Reaction. *ACS Appl. Mater. Interfaces* **2016**, *8*, 2910–2916.
- (26) McGlynn, J. C.; Dankwort, T.; Kienle, L.; Bandeira, N. A. G.; Fraser, J. P.; Gibson, E. K.; Cascallana-Matías, I.; Kamarás, K.; Symes, M. D.; Miras, H. N.; Ganin, A. Y. The Rapid Electrochemical Activation of MoTe₂ for the Hydrogen Evolution Reaction. *Nat. Commun.* **2019**, *10*, 5336.
- (27) Anantharaj, S.; Kundu, S.; Noda, S. Progress in Nickel Chalcogenide Electrocatalyzed Hydrogen Evolution Reaction. *J. Mater. Chem. A* **2020**, *8*, 4174–4192.
- (28) Hilsenbeck, S. J.; Mccarley, R. E.; Goldman, A. I.; Schrader, G. L. Hydrodesulfurization Activity and EXAFS Characterization of Novel Ternary Tin and Lanthanum Molybdenum Sulfide Catalysts. *Chem. Mater.* **1998**, 4756, 125–134.
- (29) Schewe-Miller, I. M.; Koo, K. F.; Columbia, M.; Li, F.; Schrader, G. L. Synthesis and Characterization of Lead Chevrel Phase Thin Films for Hydrodesulfurization Catalysis. *Chem. Mater.* **1994**, *6*, 2327–2335.
- (30) McCarty, K. F.; Schrader, G. L. Hydrodesulfurization by Reduced Molybdenum Sulfides: Activity and Selectivity of Chevrel Phase Catalysts. *Ind. Eng. Chem. Prod. Res. Dev.* **1984**, 23, 519–524.
- (31) Alonso-Vante, N.; Schubert, B.; Tributsch, H. Transition Metal Cluster Materials for Multi-Electron Transfer Catalysis. *Mater. Chem. Phys.* **1989**, 22, 281–307.
- (32) Fischer, C.; Alonso-Vante, N.; Fiechter, S. T. H. Electrocatalytic Properties of Mixed Transition Metal Tellurides (Chevrel-Phases) for Oxygen Reduction. *J. Appl. Electrochem.* **1995**, 25, 1004–1008.
- (33) Vante, N.; Shubert, B.; Tributsch, H.; Perrin, A. Influence of D-State Density and Chemistry of Transition Metal Cluster Selenides on Electrocatalysis. *J. Catal.* **1988**, *112*, 384–391.
- (34) Vante, N. A.; Tributsch, H. Energy Conversion Catalysis Using Semiconducting Transition Metal Cluster Compounds. *Nature* **1986**, 323, 431–432.
- (35) Vante, N. A.; Jaegermann, W. H.; Hónle, W.; Yvon, K. Electrocatalysis of Oxygen Reduction by Chalcogenides Containing

- Mixed Transition Metal Clusters. J. Am. Chem. Soc. 1987, 109, 3251–3257.
- (36) Perryman, J. T.; Ortiz-Rodríguez, J. C.; Jude, J. W.; Hyler, F. P.; Davis, R. C.; Mehta, A.; Kulkarni, A. R.; Patridge, C. J.; Velázquez, J. M. Metal-Promoted Mo₆S₈ Clusters: A Platform for Probing Ensemble Effects on the Electrochemical Conversion of CO₂ and CO to Methanol. *Mater. Horiz.* **2020**, *7*, 193–202.
- (37) Naik, K. M.; Sampath, S. Cubic Mo₆S₈-Efficient Electrocatalyst Towards Hydrogen Evolution Over Wide PH Range. *Electrochim. Acta* **2017**, 252, 408–415.
- (38) Ojha, K.; Banerjee, S.; Sharma, M.; Dagar, P. Synthesis of Chevrel Phase ($Cu_{1.8}Mo_cS_8$) in Composite with Molybdenum Carbide for Hydrogen Evolution Reactions. *Bull. Mater. Sci.* **2018**, *41*, 119.
- (39) Jiang, J.; Gao, M.; Sheng, W.; Yan, Y. Hollow Chevrel-Phase NiMo₃S₄ for Hydrogen Evolution in Alkaline Electrolytes. *Angew. Chem.* **2016**, *128*, 15466–15471.
- (40) Perryman, J. T.; Hyler, F. P.; Ortiz-Rodríguez, J. C.; Mehta, A.; Kulkarni, A. R.; Velázquez, J. M. X-Ray Absorption Spectroscopy Study of the Electronic Structure and Local Coordination of 1st Row Transition Metal-Promoted Chevrel-Phase Sulfides. *J. Coord. Chem.* **2019**, 72, 1322–1335.
- (41) Yvon, K.; Paoli, A. Charge Transfer and Valence Electron Concentration in Chevrel Phases. *Solid State Commun.* **1977**, *24*, 41–45.
- (42) Lancry, E.; Levi, E.; Gofer, Y.; Levi, M.; Salitra, G.; Aurbach, D. Leaching Chemistry and the Performance of the Mo₆S₈ Cathodes in Rechargeable Mg Batteries. *Chem. Mater.* **2004**, *16*, 2832–2838.
- (43) Borodzinski, J.; Lasia, A. Study of Hydrogen Evolution on Selected PTFE-Bonded Porous Electrodes. *Int. J. Hydrogen Energy* **1993**, *18*, 985–994.
- (44) Su, H.; Sita, C.; Pasupathi, S. The Effect of Gas Diffusion Layer PTFE Content on the Performance of High Temperature Proton Exchange Membrane Fuel Cell. *Int. J. Electrochem. Sci.* **2016**, *11*, 2919–2926.
- (45) McCrory, C. C. L.; Jung, S.; Ferrer, I. M.; Chatman, S. M.; Peters, J. C.; Jaramillo, T. F. Benchmarking Hydrogen Evolving Reaction and Oxygen Evolving Reaction Electrocatalysts for Solar Water Splitting Devices. *J. Am. Chem. Soc.* **2015**, *137*, 4347–4357.
- (46) Kibsgaard, J.; Chen, Z.; Reinecke, B. N.; Jaramillo, T. F. Engineering the Surface Structure of MoS₂ to a Preferentially Expose Active Edge Sites for Electrocatalysis. *Nat. Mater.* **2012**, *11*, 963–969.
- (47) Kresse, G.; Furthmüller, J. Efficient Iterative Schemes for Ab Initio Total-Energy Calculations Using a Plane-Wave Basis Set. *Phys. Rev. B: Condens. Matter Mater. Phys.* **1996**, *54*, 11169–11186.
- (48) Hammer, B.; Hansen, L. B.; Nørskov, J. K. Improved Adsorption Energetics within Density-Functional Theory Using Revised Perdew-Burke-Ernzerhof Functionals. *Phys. Rev. B: Condens. Matter Mater. Phys.* **1999**, *59*, 7413–7421.
- (49) Sun, J.; Ruzsinszky, A.; Perdew, J. Strongly Constrained and Appropriately Normed Semilocal Density Functional. *Phys. Rev. Lett.* **2015**, *115*, 036402.
- (50) Mathew, K.; Sundararaman, R.; Letchworth-Weaver, K.; Arias, T. A.; Hennig, R. G. Implicit Solvation Model for Density-Functional Study of Nanocrystal Surfaces and Reaction Pathways. *J. Chem. Phys.* **2014**, *140*, 084106.
- (51) Manz, T. A.; Limas, N. G. Introducing DDEC6 Atomic Population Analysis: Part 1. Charge Partitioning Theory and Methodology. *RSC Adv.* **2016**, *6*, 47771–47801.
- (52) Atkins, P. Physical Chemistry, 6th ed.; Oxford University Press, 1998.
- (53) Nørskov, J. K.; Bligaard, T.; Logadottir, A.; Kitchin, J. R.; Chen, J. G.; Pandelov, S.; Stimming, U. Trends in the Exchange Current for Hydrogen Evolution. *J. Electrochem. Soc.* **2005**, *152*, J23.
- (54) Chase, M. W. NIST-JANAF Thermochemical Tables. J. Phys. Chem. Ref. Data 1998, 25, 551.
- (55) Levin, E. E.; Grebenkemper, J. H.; Pollock, T. M.; Seshadri, R. Protocols for High Temperature Assisted-Microwave Preparation of Inorganic Compounds. *Chem. Mater.* **2019**, *31*, 7151–7159.

- (56) Parsons, R. Atlas of Electrochemical Equilibria in Aqueous Solutions. J. Electroanal. Chem. Interfacial Electrochem. 1967, 13, 471.
- (57) Barbier, M.-J.; De Becdelievre, A.-M.; De Becdelievre, J. Electrochemical Study of Tellurium Oxido-Reduction in Aqueous Solutions. *J. Electroanal. Chem.* **1978**, *94*, 47–57.
- (58) Benck, J. D.; Hellstern, T. R.; Kibsgaard, J.; Chakthranont, P.; Jaramillo, T. F. Catalyzing the Hydrogen Evolution Reaction (HER) with Molybdenum Sulfide Nanomaterials. *ACS Catal.* **2014**, *4*, 3957–3971.
- (59) Chen, Z.; Cummins, D.; Reinecke, B. N.; Clark, E.; Sunkara, M. K.; Jaramillo, T. F. Core-Shell MoO_3 - MoS_2 Nanowires for Hydrogen Evolution: A Functional Design for Electrocatalytic Materials. *Nano Lett.* **2011**, *11*, 4168–4175.
- (60) Benck, J. D.; Chen, Z.; Kuritzky, L. Y.; Forman, A. J.; Jaramillo, T. F. Amorphous Molybdenum Sulfide Catalysts for Electrochemical Hydrogen Production: Insights into the Origin of Their Catalytic Activity. *ACS Catal.* **2012**, *2*, 1916–1923.
- (61) Merki, D.; Fierro, S.; Vrubel, H.; Hu, X. Amorphous Molybdenum Sulfide Films as Catalysts for Electrochemical Hydrogen Production in Water. *Chem. Sci.* **2011**, *2*, 1262–1267.
- (62) Zeng, M.; Li, Y. Recent Advances in Heterogeneous Electrocatalysts for the Hydrogen Evolution Reaction. *J. Mater. Chem. A* **2015**, 3, 14942–14962.
- (63) Feng, W.; Pang, W.; Xu, Y.; Guo, A.; Gao, X.; Qiu, X.; Chen, W. Transition Metal Selenides for Electrocatalytic Hydrogen Evolution Reaction. *ChemElectroChem* **2020**, *7*, 31–54.